Kovove Mater. 62 2024 339–353
DOI: 10.31577/km.2024.6.339

Improving the mechanical properties and corrosion resistance of Mg-2Zn-0.5Zr-1.5Dy alloy by combining hot extrusion with subsequent fluorinated coating

Junguang He[1,2]*, Xuyang Li[1], Yuan Gong[1], Huina Shi[1], Qinglei Gao[1], Jiuba Wen[1,2], Huan Li[1]

[1] *School of Materials Science and Engineering, Henan University of Science and Technology, Luoyang 471023, P. R. China*
[2] *Provincial and Ministerial Co-construction of Collaborative Innovation Center for Non-ferrous Metal New Materials and Advanced Processing Technology, Luoyang 471023, P. R. China*

Received 19 July 2024, received in revised form 17 October 2024, accepted 7 November 2024

Abstract

A novel Mg-2.0Zn-0.5Zr-1.5Dy (wt.%) alloy used for orthopedic applications was prepared by hot extrusion deformation, followed by fluorinated coating treatment. The corrosion behavior, film formation mechanism, and corrosion resistance of as-cast, extruded (E460), and coated (CE460) specimens were investigated. Results demonstrated that the grain size after extruding was refined significantly, and the mechanical properties improved greatly while the corrosion resistance decreased slightly. The average corrosion rate of extruded sample E460 immersed in simulated body fluid (SBF) for 240 hours was about 1.030 $\pm$ 0.017 mm y^{-1}, and the yield strength (YS), ultimate tensile strength (UTS), and elongation (EL) were 310 $\pm$ 17 MPa, 321 $\pm$ 25 MPa, 11.1 $\pm$ 1.9 %, respectively. CE460 specimen was treated by combining hot extrusion with subsequent fluorinated coating; the mechanical properties changed less, whereas the corrosion resistance increased dramatically, and its average corrosion rate decreased from 1.03 $\pm$ 0.017 to 0.070 $\pm$ 0.004 mm y^{-1}. The comprehensive performance was improved greatly by combining hot extrusion with subsequent fluorinated coating. The corrosion mechanism for specimens under extruded and annealed conditions was analyzed.

K e y w o r d s: bio-magnesium alloy, hot extrusion, fluorinated coating, corrosion resistance

1. Introduction

Magnesium alloys are suitable for implanting biomedical materials due to their favorable biocompatibility, biodegradability, and elastic modulus, similar to human bone tissue [1–4]. Nevertheless, the principal drawback of using magnesium alloys as implants lies in the rapid degradation rate in the physiological environment and the production of hydrogen gas at a rate the body cannot regulate [5]. Extensive investigations have been performed to improve its corrosion resistance, such as alloying, heat treatment, thermal deformation, and coating treatment [6–8].

Composition design particularly provides a scientific basis for developing biodegradable Mg alloys. Zn, an essential trace element for the human body, can promote the growth of human bone cells and help bone healing [9]. Zr is completely biocompatible, exhibits a great grain refining effect, and improves the corrosion resistance of Mg alloys to a remarkable extent [10]. However, adding Zr to Mg should be less than 1 % because a higher content of Zr may lead to severely reduced corrosion resistance [11]. In addition, the appropriate addition of rare earth elements can significantly improve the mechanical properties, purify impurities, increase the matrix potential, forms a stable protective film, and improves the corrosion resistance of Mg alloys [6, 12]. The toxicity of Dy is reported to be lower than that of other commonly used rare earth elements, such as Nd, Y, La, and Pr [13, 14]. Our research group has recently developed a novel Mg-2Zn-0.5Zr-1.5Dy (wt.%) alloy [14]. Although the as-cast Mg-2Zn-0.5Zr--1.5Dy (wt.%) alloy has good corrosion resistance,

*Corresponding author: e-mail address: he.ellen@163.com

its comprehensive performance needs further improvement.

Generally, the microstructure of as-cast magnesium alloy is not uniform. The grain size of the alloy is large, and composition bias exists in the microstructure, which is not conducive to the development of the mechanical properties and corrosion resistance of the as-cast alloy [15, 16]. Hot extrusion is an important method to improve the microstructure and properties of magnesium alloys. It can give the alloy a refined and uniform microstructure so that the extruded alloy has higher strength and plasticity [17, 18]. However, this treatment concurrently diminishes its corrosion resistance, rendering it suboptimal for biomedical applications. Surface modification techniques offer a promising solution to this issue. These methods can produce a variety of coatings, including inorganic, polymeric, and composite [19–22].

Therefore, the hot extrusion process should combine with alloying and surface modification methods to further improve the mechanical properties and corrosion resistance of the alloy [23]. Mao et al. found that the volume of hydrogen evolution of JDBM coated with MgF_2 in the artificial plasma solution was lower than that of untreated JDBM [24]. Studies indicated that MgF_2-coated treatment could reduce the degradation rate of Mg-Zn-Zr alloy without adversely affecting cells and tissues and exhibit better biocompatibility [25]. Riaz et al. found that the current density and hydrogen evolution rate of ZK60 alloy with the MgF_2 coated were significantly reduced [26]. However, fluoride conversion coating has been studied extensively to control the degradation rate of magnesium. Nevertheless, most of them were based on pure Mg or AZ series magnesium alloys.

In this paper, based on the as-cast Mg-2Zn-0.5Zr--1.5Dy (wt.%) alloy, hot extrusion and hydrogen fluoride treatments were carried out, and their effects on the mechanical properties and corrosion resistance of the alloy were investigated to improve its comprehensive properties further.

2. Material and methods

2.1. Material preparation

The nominal composition of the experimental alloy is Mg-2Zn-0.5Zr-1.5Dy (wt.%). The raw materials were melted in a corundum crucible in a vacuum induction melting furnace under the protective gas of 1 % SF6 + 99 % CO_2 (vol.%) at approximately 740 ℃ and then poured into a metal mold preheated at 200 ℃. The ingot was heated to 460 ℃ and was extruded into a rod named E460. The extrusion ratio and speed are 7.7 and 5 mm s^{-1}, respectively. The test surfaces are parallel to the extrusion direction (ED).

To further improve the corrosion resistance of the extruded alloy, part of the polished extruded samples was subsequently immersed in 30 wt.% HF solution for 72 hours at room temperature (named CE460), then rinsed with alcohol and distilled water and dried in a drying oven.

2.2. Microstructure characterization

The samples were ground successively to 2000 grit by SiC paper, polished with 1.5 μm diamond paste, followed by etching in a solution of 5 g picric acid + 100 mL ethanol + 5 mL glacial acetic acid + 10 mL deionized water. The microstructure and surface morphology were characterized using an optical microscope (OM, OLYMPUS) and scanning electron microscope (SEM, JSML5610LV).

The phase composition was detected by X-ray diffraction analysis (XRD, Bruker D8 Advance) with Cu Kα radiation. The tube voltage and current were 35 kV and 40 mA, respectively; the scanning speed was 2° min^{-1}, and the scanning range was 15°–85°.

The samples for transmission electron microscope (TEM, JSM-2010) observation were thinned approximately 100 μm using mechanical methods and cut into circular thin foils 3 mm in diameter. Then, they were prepared by twin-jet electrolytic polishing in 3 wt.% $HClO_4$ solution cooled to –40 ℃ using liquid nitrogen with a voltage and current of 80 V and 20 mA.

2.3. Tensile testing

The tensile specimens were processed into dog bone with a thickness of 2 mm, 3.5 mm in width, and 15 mm gauge length based on the GB/T 228.1-2010 standard. Tensile tests at room temperature were carried out on a Shimadzu AG-1250KN testing machine; the tensile rate was 1 mm min^{-1}, and five parallel samples were tested for each alloy.

2.4. Immersion experiment

Immersion experiments were performed in SBF with a size of ø 18 mm × 5 mm. The SBF-volume/sample-area ratio was 30 mL cm^{-2}, the liquid temperature was kept at about 37 ± 0.5 ℃, the pH was adjusted to 7.6 ± 0.2 and immersed for 240 hours with replacing SBF every 24 hours. The amount of hydrogen evolution was recorded every day using a gas-collecting device. The chemical composition of SBF is listed in Table 1. During the immersion experiment, Mg dissolution and H_2 evolution occur simultaneously. Therefore, the corrosion rate of the alloy can be calculated by hydrogen evolution volume. The calculation formula Eq.(1) of the corrosion rate P_H (mm y^{-1}) of hydrogen evolution is as follows [27]:

Table 1. Chemical composition of the SBF ($g\,L^{-1}$)

NaCl	$CaCl_2$	KCl	$NaHCO_3$	$MgCl_2 \cdot 6H_2O$	$C_6H_{12}O_6$	$Na_2HPO_4 \cdot 12\ H_2O$	KH_2PO_4	$MgSO_4 \cdot 7H_2O$
8.00	0.14	0.40	0.35	0.10	1.00	0.06	0.06	0.06

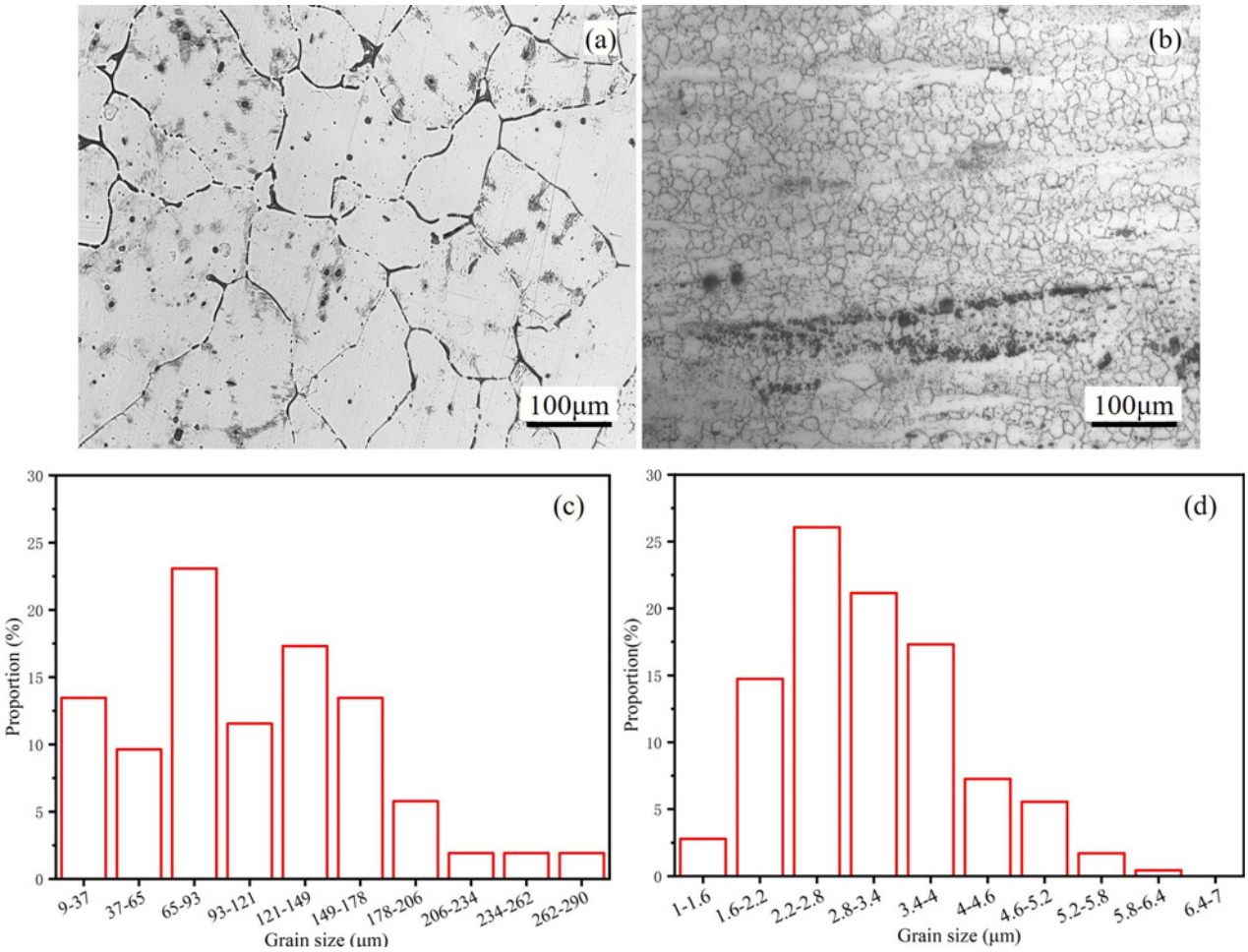

Fig. 1. Optical images and grain size distribution of Mg-2Zn-0.5Zr-1.5Dy alloys with different states: (a) as-cast, (b) E460, (c) grain size distribution of as-cast sample, and (d) grain size distribution of E460 sample.

$$P_H = (K \times V_H)/(A \times \rho \times D), \quad (1)$$

where K is a constant coefficient ($K = 95.36$), V_H is the volume of hydrogen collected (mL), A is the sample surface area (cm^2), T is the soaking time (h), and ρ is the alloy density ($g\,cm^{-3}$). Three samples from each group were tested.

2.5. Electrochemical testing

Electrochemical experiments were performed by an electrochemical workstation (Autolab, AUT84580) in a three-electrode electrochemical cell. Samples with a size of ø 11.3 mm × 8 mm were used as working electrodes, a graphite sheet as a counter electrode, and a saturated calomel electrode as a reference electrode. The electrochemical impedance spectroscopy (EIS) was recorded after the sample was immersed in SBF for 1 hour with an excitation voltage of 5 mV in the scan frequency range from 10 kHz to 0.1 Hz. Then, the polarization curve was carried out at a constant voltage scan rate of 5 mV s^{-1} in a scan scope from –1.9 to –1.1 V.

3. Results and discussion

3.1. Microstructure characterization

Figure 1 shows the optical images and grain size distribution of Mg-2Zn-0.5Zr-1.5Dy alloy with different states. The grain size of the as-extruded sample

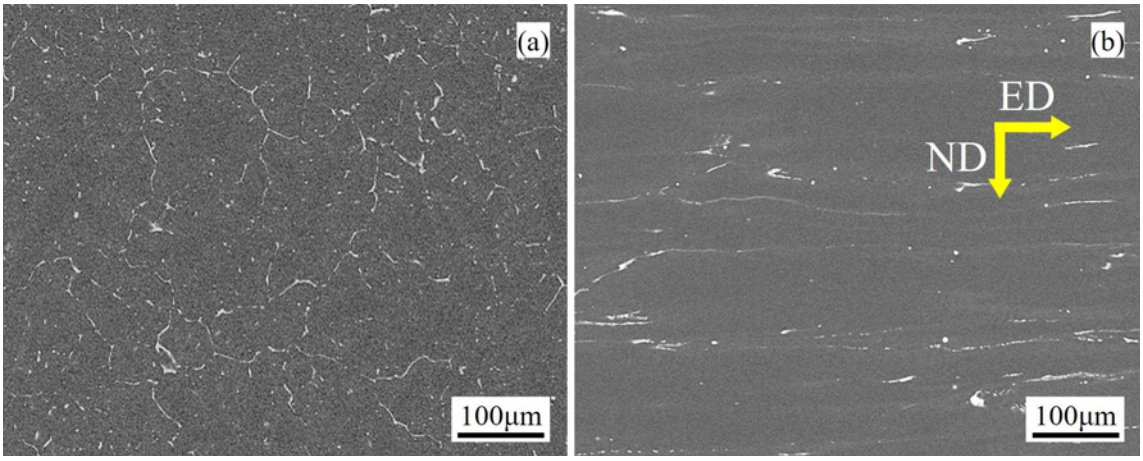

Fig. 2. Backscattered electron images of Mg-2Zn-0.5Zr-1.5Dy alloys with different states: (a) as-cast and (b) E460.

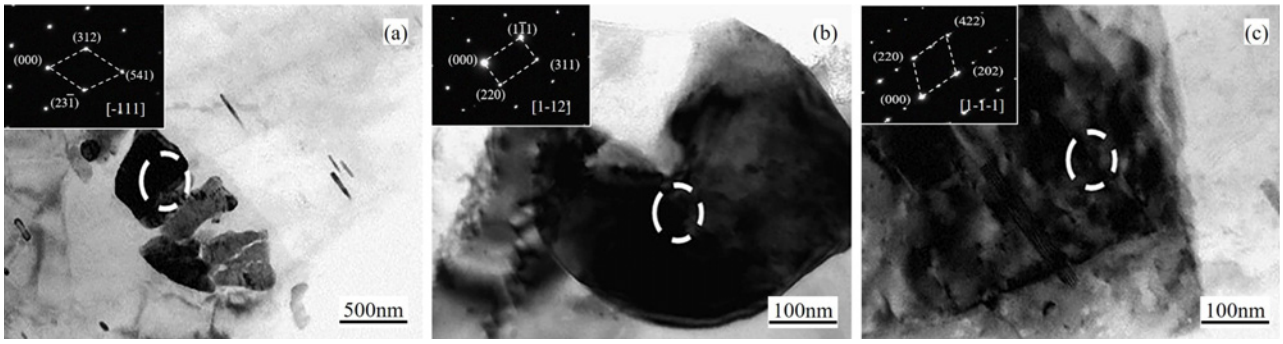

Fig. 3. TEM bright field micrograph and SAED patterns of E460 specimen: (a) the blocky phase Mg_2Zn_{11}, (b) the bone-like phase $DyMg_x$, and (c) the rod-like phase $Mg_3Dy_2Zn_3$.

was significantly refined compared with that of the as-cast sample. The as-cast alloy consisted of equiaxed crystals with an average grain size of about 110 μm; the grain size was not uniform and mainly between 9–178 μm as shown in Figs. 1a and 1c. The as-extruded sample was constituted of tiny dynamic recrystallized grains (DRGs), mainly between 2–5 μm, with several elongated deformed grains along the ED. The average grain size of DRGs for E460 decreased to about 3.0 μm, the black second phase distributed along the deformed grain boundaries, as seen in Figs. 1b and 1d. As for a large amount of fine grains in the as-extruded sample E460, a large extrusion ratio ($\lambda = 7.7$) can generate a large deformation degree, high deformation energy, and increase the nuclei number of new grains, ensuring the occurrence of dynamic recrystallization (DRX) [28]. Low deformation speed (5 mm s^{-1}) is favorable for the nucleation and growth of new grain [29]. Low extrusion temperature not only guarantees the occurrence of DRX but also prevents the easy growth of DRGs.

Figure 2 presents the backscattered electron images of Mg-2Zn-0.5Zr-1.5Dy alloys with different states. The SEM images show an obvious difference in the distribution and volume fraction of the second phases in the samples. Net-like and strip-like second phases in as-cast samples are distributed chiefly along the grain boundary areas, either continuous or semi-continuous. Granular-like second phases were found in the matrix and grain boundaries. Meanwhile, the granular-like second phases in the grain almost disappeared after extrusion and may have been dissolved into the matrix during heat treatment. Those at the grain boundaries were reduced and distributed along the elongated grain boundary. Net-like and strip-like second phases in as-extruded sample E460 were broken and partially dissolved in the matrix, and the remainder gradually became thinner with a semi-continuous network distributed along the extrusion direction. The volume fraction of the second phase in the alloy decreased from 1.79 to 1.53 % after extrusion.

Figure 3 exhibits the TEM images and selected area electron diffraction spots (SAED) of specimen E460. The blocky granular in Fig. 3a had a cubic structure, the diffraction spectrum had a good correspondence with the (312) (23–1) (541) crystal plane of the Mg_2Zn_{11} phase, and the crystal ribbon axis was [–111]. The massive bone-like particles in Fig. 3b corresponded to the (1–11) (220) (311) crystal plane of $Mg_3Dy_2Zn_3$ phase, and the corresponding ribbon

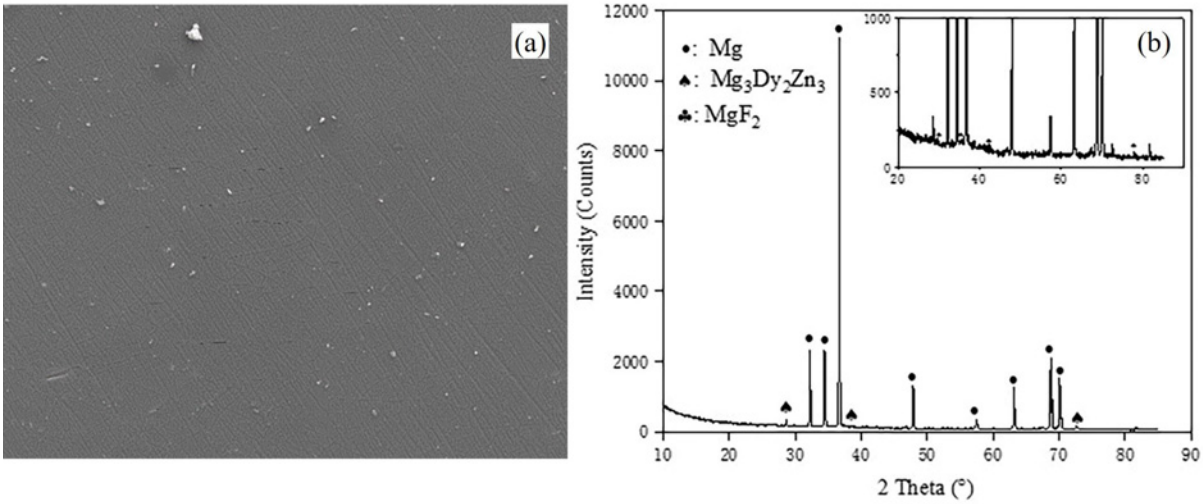

Fig. 4. SEM image (a) and X-ray diffraction pattern (b) of the CE460 sample.

Table 2. Mechanical properties of the different samples

Samples	YS (MPa)	UTS (MPa)	EL (%)
As-cast	84 ± 7	154 ± 12	8.6 ± 0.3
E460	310 ± 17	321 ± 25	11.1 ± 1.9
CE460	308 ± 14	317 ± 21	10.7 ± 1.2

axis was [–112]. The rod-like particles in Fig. 3c corresponded to the (220) (202) (422) crystal plane of $DyMg_x$, and the crystal ribbon axis was [1–1–1]. It could be determined that the second phases in the E460 specimen were mainly Mg_2Zn_{11}, $DyMg_x$, and $Mg_3Dy_2Zn_3$.

Figures 4 and 5 show the surface micromorphology, XRD spectra, and the cross-sectional morphology of the as-extruded specimen immersed in 30 % HF solution for 72 h (CE460 sample). The coating was relatively thin, which was evident from the polishing marks underneath the coating [30], and part of the second phase can be seen in Fig. 4a. Except for the magnesium matrix, $Mg_3Dy_2Zn_3$ and MgF_2 phases were detected by the XRD pattern in Fig. 4b. This indicates that an MgF_2 coating layer has formed on the CE460 specimen surface due to the high concentration of fluoride, the long immersion duration, and the low reaction temperature [31]. The surface scanning map, cross-section morphology, and scan map of the CE460 sample are shown in Fig. 5. The CE460 surface was mainly composed of Mg, F, O, Zn, and Dy from Fig. 5a. The thickness of MgF_2 coating was about 8 μm from the cross-section map. Faramoushjan et al. [32] made a similar observation in their studies related to Mg-Ca-Zn alloy. It could be seen from the line scan maps that the outer edge of the coating was mainly composed of Mg and O, and the inner side of the coating mainly contained Mg and F elements; however, O and F almost disappeared in the substrate, Mg content increased rapidly and remained stable, and Dy and Zn content were relatively stable. It could be inferred that the outer part of the coating is mainly MgO and the inner part is MgF_2.

3.2. Mechanical properties

Table 2 displays the mechanical properties of as-cast, E460, and CE460 samples. It can be seen that the mechanical properties of the as-extruded E460 sample are greatly improved compared with those of the as-cast sample. The YS, UTS, and EL of as-cast samples were 84 ± 7 MPa, 154 ± 12 MPa, and 8.6 ± 0.3 %, respectively. Those of the E460 sample increased remarkably to 310 ± 17 MPa, 321 ± 25 MPa, and 11.1 ± 1.9 %. The mechanical performance of the CE460 sample with fluoride coating has changed little compared with that of the E460 sample.

According to the Hall-Petch formula: $\sigma_s = \sigma_0 + kd^{-1/2}$, where σ_0, k, and d are the lattice friction force, Petch slope, and grain diameter, respectively. YS increases with decreasing grain size, confirmed by an abundant investigation based on diverse alloy systems [33, 34]. In this paper, the average grain size was reduced from 110 μm of the as-cast sample to 3.0 μm of the E460 sample. The diminution of grain size after extrusion results in strength improvement. Compared with aluminum alloys and steel, Mg alloys with insuf-

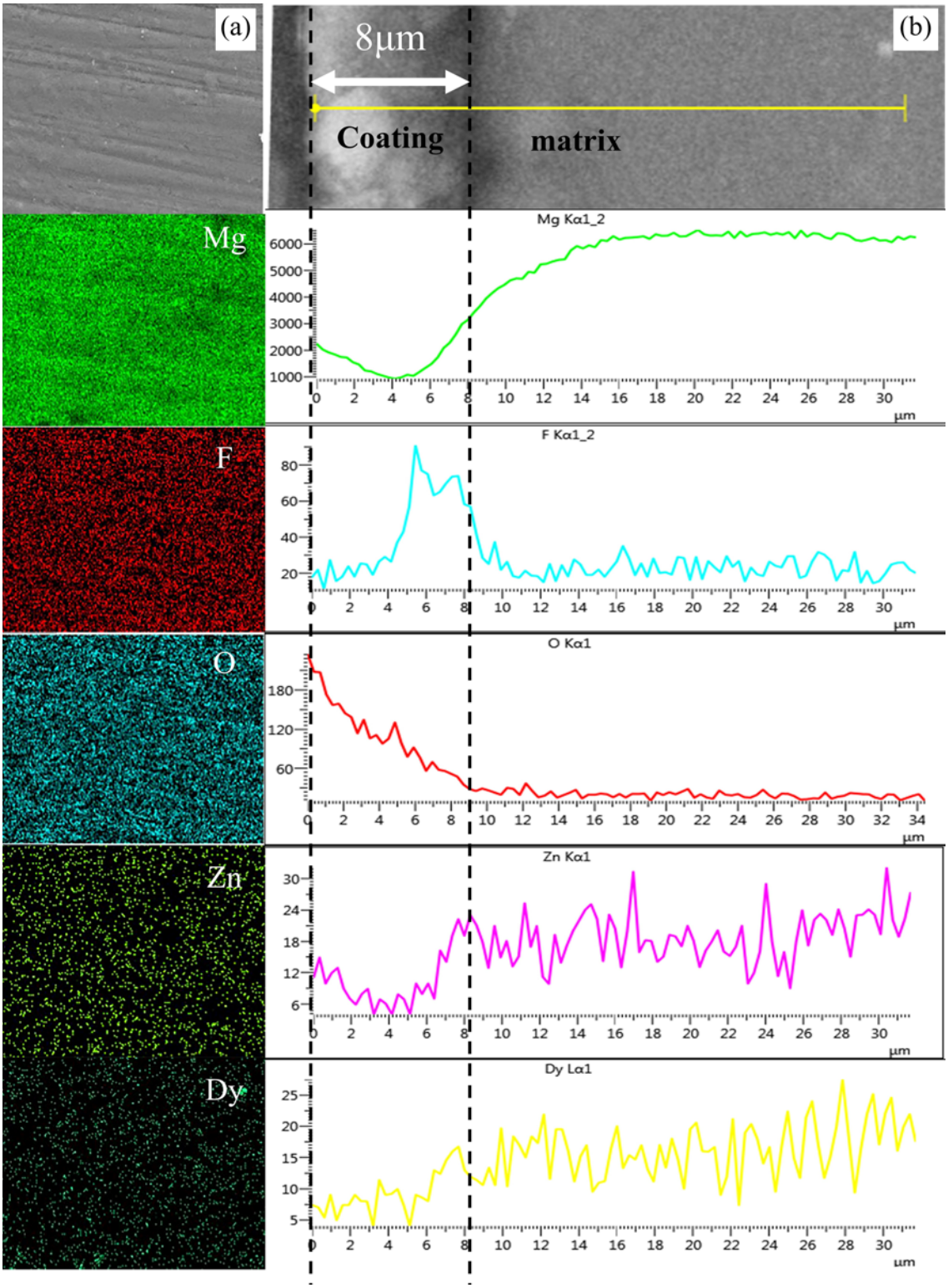

Fig. 5. Surface topography and its scanning map (a), cross-section morphology and line scan map (b) of the CE460 sample.

ficient slip systems exhibit a larger value of k. Therefore, grain refinement can improve the strength more effectively [35].

The increasing grain boundaries caused by grain refinement bring about strong obstacles inhibiting the internal dislocation movement in the initial stage of plastic deformation, and the dislocation plugging leads to an increase in the difficulty of slippage of adjacent grains, markedly promoting the yield strength [36, 37]. Moreover, the formation of texture caused by hot ex-

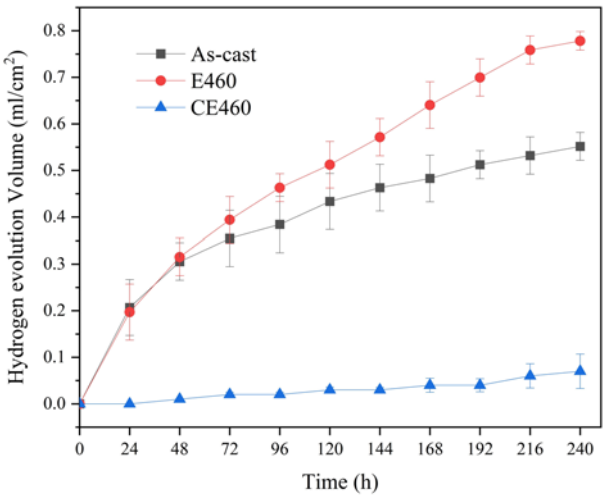

Fig. 6. Variation curves of hydrogen evolution volumes of as-cast, E460, and CE460 samples with immersion time from 0 to 240 hours.

trusion can contribute to strength, which limits the activity of basal slip when tensile behavior happens [38]. In addition, the fine grain size can increase the basic and angular slip systems, which promotes grain boundary sliding and torsion, shortens the dislocation movement distance and greatly improves plasticity [39]. Furthermore, the small and uniform grain size is also conducive to the better coordination and transmissibility of the deformation between different grains, thus giving it better plasticity [40]. Therefore, the mechanical performance of E460 and CE460 specimens was relatively better.

3.3. Corrosion resistance

Figure 6 reveals the hydrogen evolution results of samples after being immersed in SBF for 240 hours. The hydrogen evolution volume of the as-cast sample continued to increase with the extension of the immersion time; it increased to 0.55 mL cm^{-2} as the immersion time reached 240 hours. The increasing trend of hydrogen evolution of the E460 sample was similar to that of the as-cast sample, but the hydrogen evolution volume increased to 0.78 mL cm^{-2} as the E460 sample was immersed in SBF for 240 hours. However, the hydrogen evolution volume of the CE460 specimen was almost zero in the first 192 hours; it increased slowly later and increased to about 0.06 mL cm^{-2} as the immersing time up to 240 hours, which was far below that of as-cast and E460 samples.

The corrosion rates of the samples immersed in SBF for 240 h can be obtained according to the calculation formula of the P_H, the results of which are shown in Table 3. The average corrosion rate of the as-cast sample was 0.740 ± 0.011 mm y^{-1}. After extrusion, the average corrosion rate of the E460 specimen increased to 1.030 ± 0.017 mm y^{-1}. After further MgF_2 coating treatment, the average corrosion rate of the CE460 specimen decreased significantly, about 0.070 ± 0.004 mm y^{-1}.

Figure 7 exhibits the corrosion morphologies of the samples immersed in SBF for 240 hours. There were many white flocculent corrosion products and cracks on the as-cast sample surface, implying serious corrosion, as shown in Fig. 7a. The E460 sample surface had a very thick corrosion products layer and many cracks still, indicating the corrosion, as seen in Fig. 7b. How-

Table 3. The average corrosion rate of the different samples immersed in SBF for 240 hours

Samples	As-cast	E460	CE460
Corrosion rate (mm y^{-1})	0.740 ± 0.011	1.030 ± 0.017	0.070 ± 0.004

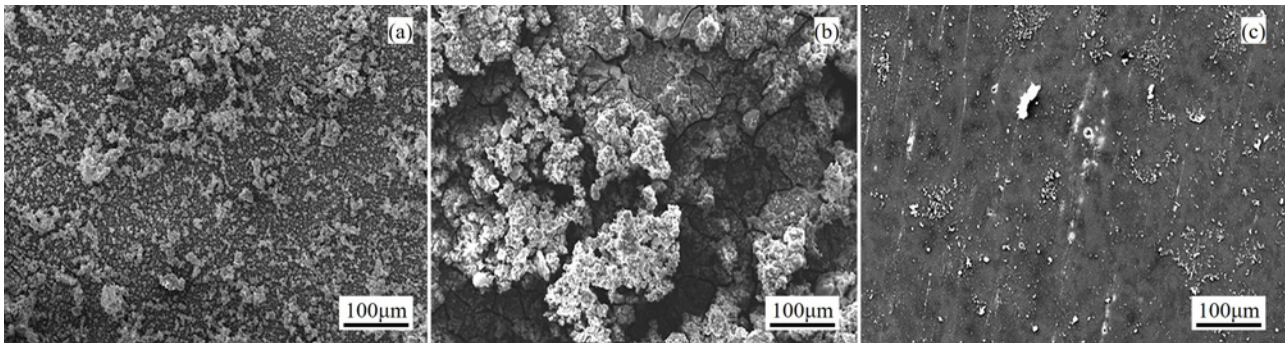

Fig. 7. Corrosion morphologies of the investigated samples after immersion in SBF for 240 hours: (a) as-cast, (b) E460, and (c) CE460.

ever, the corrosion of CE460 sample was significantly lighter and had only a small amount of corrosion products, and cracks caused by corrosion products were invisible on the surface. Meanwhile, the white strip corrosion and pit corrosion distributed along the extrusion direction, as shown in Fig. 7c.

The potential of the second phase was higher than that of the Mg matrix, and the maximum potential difference between them was close to 95 mV [41]. The second phase, composed of $DyMg_x$, Mg_2Zn_{11}, and $Mg_3Dy_2Zn_3$, will likely form galvanic corrosion with the matrix. The volume fraction of the second phases in the alloy after extrusion decreased from 1.79 to 1.53 %, which was beneficial in slowing down the local corrosion of the alloy [42, 43]. Furthermore, several studies reported that the difference in crystal structure between MgO and the internal Mg matrix will be reduced after grain refinement, and MgO film will tend to be stable and dense, thus improving the corrosion resistance of Mg alloys [44–46]. Grain refinement increases grain boundary length, promoting oxide film conduction and formation rate, and grain boundaries act as a corrosion barrier and can retard corrosion kinetics [47, 48]. However, an increase in dislocation density generated by deformation can reduce the equilibrium potential near the dislocation, enhancing the thermodynamic driving force of electrochemical corrosion [49, 50]. Moreover, dislocations distort the lattice, and atoms in the distorted lattice are more active than those in the normal lattice and are susceptible to corrosion [51]. Therefore, a high dislocation density can decrease the corrosion resistance of alloys by corrosion, preferably at the outcrop of the dislocations [52, 53]. Some studies indicated that the tensile residual stress induced by processing could impart cracks or defects in alloys and decrease the activation energy for an atom to escape from the lattice and get into the solution. In addition, the tensile residual stress could reduce the corrosion potential and enhance thermodynamic activity. Therefore, corrosion is accelerated when tensile residual stress exists on the alloy surface [54–56]. The stress corrosion of the extruded alloy due to the internal stress generated by the deformation is not conducive to the corrosion resistance of the alloy [57–59]. The synthetic action of these factors makes the corrosion rate of the as-extruded samples higher than that of the as-cast sample.

The corrosion rate of the CE460 specimen is noticeably lower than that of other specimens for the entire stage. This indicated that MgF_2 film on extruded samples could act as a corrosion-barrier coating and cause a declined corrosion rate [32]. The outer MgF_2 layer of the CE460 specimen prevents the direct contact of the Mg matrix with SBF and greatly slows down the corrosion rate of the alloy in the initial time of the experiment. With increasing immersion duration, a compact $Ca_3(PO_4)_2$ layer is formed on the CE460 sample surface due to PO_4^{3-} deposition induced by F^- and Ca^{2+} deposition caused by Mg^{2+}, and the newly generated surface film instead of MgF_2 will continue to protect the matrix [60]. However, the strip-shaped second phase in the grain boundary is less likely to react with HF solution than the Mg matrix; the coating thickness in this position is thinner. As the soaking time increases even further, SBF breaks through the coating in the second phase and reacts with the alloy. Therefore, the initial corrosion marks of the CE460 specimen with MgF_2 coating are distributed along the extrusion direction.

As the immersing time went on, it was more and more difficult for the corrosion medium to get into the magnesium alloy substrate, so the degradation rate decreased generally to achieve stability. Compared with the degradation of bare magnesium alloy in a corrosion medium, the magnesium alloy with fluoride conversion coating owned a dense protective coating, which could separate the alloy substrate from the corrosion surrounding and decrease the degradation rate of the alloy.

At the beginning of soaking in SBF, MgO in the outer coating reacted in solution to precipitate $Mg_3(PO_4)^2$ because the solubility product of $Mg_3(PO_4)^2$ (1.04×10^{-22}) is much less than that of MgF_2 (5.16×10^{-3}), it was gradually replaced by $Ca_3(PO_4)^2$ due to its solubility product (2.07×10^{-33}). Meanwhile, the SBF solution probably moved through the MgF_2 coating along the MgF_2 columnar grain boundaries. Mg in substrate reacted with SBF solution, the solid corrosion products fulfilled the microchannel in the MgF_2 grain boundaries and acted as a barrier between SBF solution and Mg substrates and held back the further reaction, and the corrosion process was slowed down. The increase in corrosion products and evolved H_2 gas caused internal pressure (due to the higher volume when compared to the substrate) on the AZ61/fluoride conversion coating interface and tension forces in the coating. If the pressure reaches a certain critical value, it causes a fracture of the fluoride conversion coating. Across a fracture of the fluoride conversion coating, the SBF solution can penetrate the base material, resulting in corrosion reactions. Due to the creation of the microcell, the corrosion attack starts with a higher intensity, and the AZ61 alloy corroded rapidly.

3.4. Electrochemical properties

The polarization curves of as-cast, E460, and CE460 samples immersed in SBF for 1 hour are shown in Fig. 8. The self-corrosion potential (E_{corr}), breakdown potential (E_b), and self-corrosion current density (I_{corr}) derived from the polarization curves by Tafel extrapolation method are presented in Table 4. The E_{corr} of as-cast sample was –1.66 V (SCE). The

Table 4. Experimental results from Tafel curves in Fig. 8

Samples	E_{corr} (V vs. SCE)	I_{corr} (μA cm^{-2})	P_i (mm y^{-1})
As-cast	–1.66	3.55	0.090
E460	–1.38	3.91	0.099
CE460	–1.42	0.316	0.008

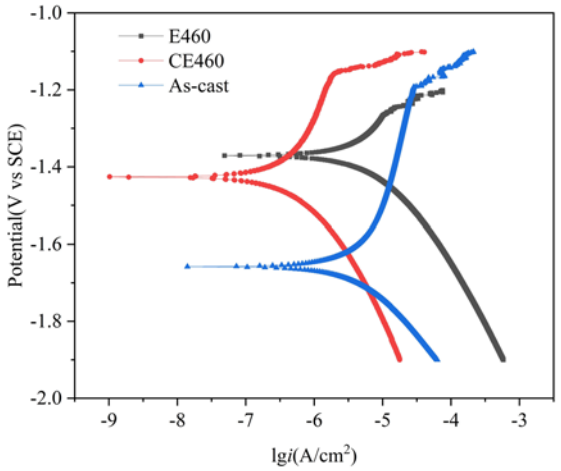

Fig. 8. Polarization curves of the investigated samples immersed in SBF for 1 hour.

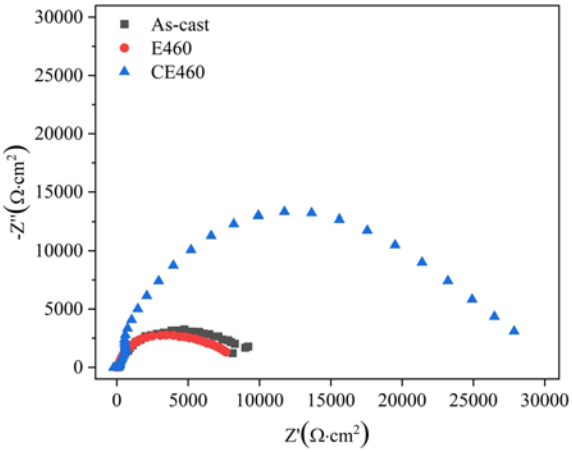

Fig. 9. Impedance diagrams of as-cast, E460, and CE460 samples immersed in SBF for 1 hour.

E460 and CE460 samples revealed more positive E_{corr} than the as-cast samples. After extrusion, the E_{corr} of the alloy shifted positively, obviously to −1.44 V (SCE). Whereafter further HF coating treatment, the E_{corr} of the alloy changed a little, appr. –1.42 V (SCE). The results for the E460 sample are inconsistent with the previous PH. The elevation of E_{corr} indicates that the electrochemical corrosion tendency of the alloys becomes smaller according to thermodynamics, but it cannot be estimated for its corrosion resistance. The corrosion resistance depends on the corrosion rate.

I_{corr} reflects the corrosion rate of the alloy. The smaller the I_{corr} value, the lower the corrosion rate [61]. The I_{corr} of as-cast and E460 specimens was 3.55 and 3.91 μA cm^{-2}, respectively, implying extrusion deformation led to an increased corrosion rate. That of CE460 sample with MgF_2 coating was about 0.316 μA cm^{-2}, reducing one order of magnitude. It indicates that the corrosion rate of the CE460 sample was much lower than that of the as-cast and E460 specimens. The large decrease in the I_{corr} value of CE460 indicates the ability of MgF_2 coating to serve as a barrier layer, thus preventing the permeation of erosive ions present in SBF and slowing down the corrosion rate of the alloy [30, 62]. Given the thermodynamics and dynamics, the CE460 sample with fluorinated coating has a much better corrosion resistance than others.

The degradation rate of the specimens could also be calculated by the I_{corr} value using the following formula [63]:

$$P_i = 3270\frac{I_{corr}}{\rho V}M, \tag{2}$$

where P_i is the degradation rate (mm y^{-1}), I_{corr} is the corrosion current density (A cm^{-2}), M is the molecular weight of the Mg alloy (g), V is the number of electrons lost during the oxidation reaction, and ρ is the measured density of the Mg alloy (g cm^{-3}). It was shown that the corrosion rates obtained by I_{corr} were consistent with those obtained by hydrogen evolution, but for all specimens, those obtained by I_{corr} were markedly lower than those determined by hydrogen evolution. Shi et al. [64, 65] found similar results for instantaneous corrosion rate. This could be caused by P_i being the instantaneous corrosion rate for 1 h, whereas P_h is the average corrosion rate for 10 days. On the other hand, the P_i for specimen CE460 was the lowest among all other specimens.

The impedance diagrams of as-cast, E460, and CE460 samples immersed in SBF for 1 hour are shown in Fig. 9. The Nyquist plots of as-cast, E460, and CE460 samples consist of only a single semicircle capacitive loop. The corrosion resistance of the alloys is usually based on the magnitude of the capacitive arc modulus. The larger the modulus is, the greater the reaction resistance and the slower the anode alloy corrosion is [66–68]. According to the impedance curve, the value of the resistance arc is CE460 > as-

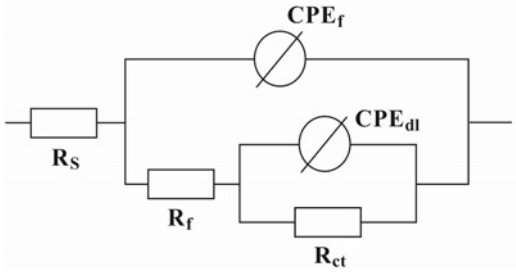

Fig. 10. Equivalent electrical circuit used to fit the EIS data obtained on the as-cast and E460 samples (a) and CE460 sample (b) in SBF.

-cast > E460. The capacitive arc radius of the CE460 is far bigger than that of the E460 and as-cast samples. Therefore, the CE460 sample has the best corrosion resistance.

3.5. Corrosion behavior

The corrosion behavior of Mg-2.0Zn-1.0Dy-0.5Zr alloys with different states in SBF shows distinct differences. Based on the immersion experiments and electrochemical tests, corrosion models of as-cast, extruded, and coated specimens in SBF are proposed in Fig. 11.

When the as-cast sample is immersed in SBF for a period of time, the defects in the oxide film, such as micro-cracks, scratches, etc., due to its loose structure, chloride ions preferably penetrate the membrane structure and react with $Mg(OH)_2$ and MgO to form the active part [69]. After that, micro galvanic corrosion occurs immediately due to the potential difference between the second phase and the matrix, with the second phase acting as the micro-cathode and the Mg-matrix acting as the micro-anode. The α-Mg matrix adjacent to the second phases (mainly Mg_2Zn_{11}, $DyMg_x$, and $Mg_3Dy_2Zn_3$) region at the grain boundary dissolves preferentially in SBF solution because most of which are distributed along the grain boundary (Fig. 2a). Subsequently, the corrosion develops along the grain boundary into the grain, and the corrosion products crack due to the accumulation of hydrogen generated by the corrosion, which leads to the leakage of α-Mg matrix and the corrosion continues to expand inward. With the gradual increase of the corrosion layer thickness, the second phase, with the coarse and uneven distribution, accelerates the micro galvanic corrosion, and the cracking of the corrosion layer releases a large stress on the interior. Which not only reduces the obstruction of the second phase on the matrix surface, accelerates the lateral expansion, but also advances the longitudinal depth of the corrosion reaction, finally forming the corrosion morphology shown in Fig. 7a. Schematic diagrams of the corrosion process of the as-cast sample are shown in Figs. 11a1–a2.

The extruded E460 specimen, compared with the as-cast sample, has a high dislocation density and residual stress, which results in a substantial increase in active sites. So aggressive ions locally preferably attack the dislocation outcrop as the extruded E460 specimen is immersed in SBF, forming a lot of microscopic corrosion on the oxide surface. Under residual tensile stress (i.e., corrosion booster), the corrosion rapidly spreads from the surface into the specimen interior. Many micro-galvanic couples are established immediately when the oxide film is destroyed and the inner Mg-matrix is in contact with the SBF solution, resulting in the extruded specimen accelerated corrosion [70]. The corrosion propagates in succession along the regions with lower potential and weaker passive layers, forming further corrosion deterioration with increasing immersion time. Finally, the extruded E460 specimen was corroded badly, as shown in Fig. 7b. Schematic diagrams of the corrosion behavior of the extruded E460 specimen are shown in Figs. 11b1–b2.

As the CE460 specimen was immersed in SBF solution, MgO in the outer coating prevents the direct contact of the MgF_2 with SBF. Whereafter, aggressive ions locally penetrated through the outer coating to the inner MgF_2 layer and reacted with MgF_2 to transform $Mg(OH)_2$. Meanwhile, the smaller SBF solution moved through MgF_2 coating along the MgF_2 columnar grain boundaries, arrived at the substrate, and reacted with Mg substrates. The solid corrosion products fulfilled the microchannel in the MgF_2 grain boundaries, acted as a barrier between SBF solution and Mg substrates, and held back the further reaction; the corrosion process was slowed down. The quantity of corrosion products and evolved H_2 gas was elevated as immersing time went on; it caused internal pressure on the substrates/coating interface and tension forces in the coating. As the pressure reached a critical value, it resulted in the fracture of the MgF_2 coating, increased the area of corrosion attack, and increased Mg substrates corroded with a higher intensity. Moreover, due to its dissolution, the MgF_2 coating became looser than the original dense coating. Aggressive ions penetrated through the loose MgF_2 coating to the substrates and corroded the Mg substrates. The schematic diagrams of the corrosion behavior of the CE460 specimen in SBF solution are shown in Figs. 11c1–c2.

4. Conclusions

The grain size of Mg-2Zn-0.5Zr-1.5Dy alloy after extruded treatment is refined through dynamic recrystallization; the mechanical properties of the alloy are improved significantly, but the corrosion resistance is reduced. The YS, UTS, EL, and corrosion rate of E460

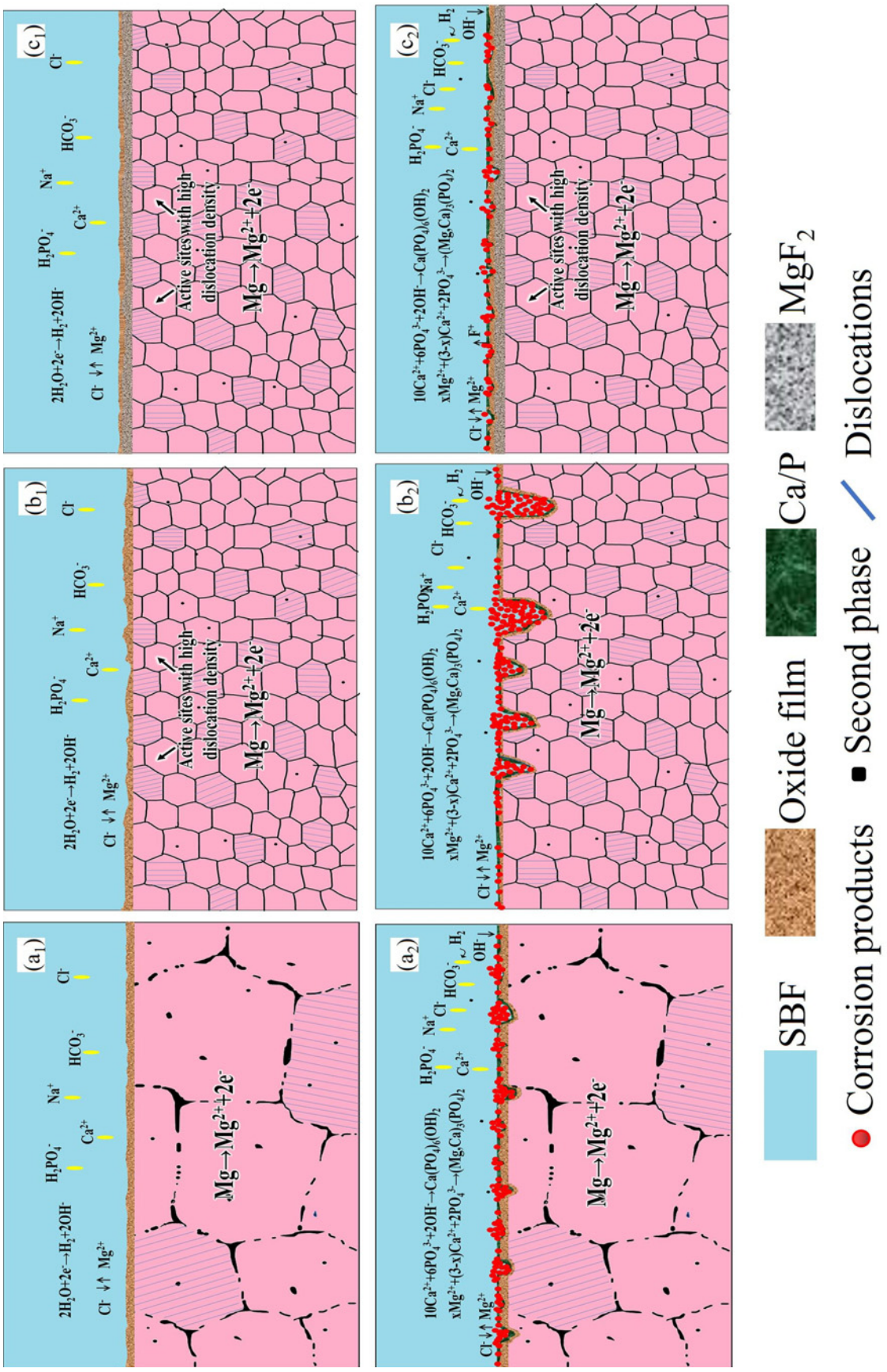

Fig. 11. Schematic diagrams of the corrosion behavior of the as-cast (a1, a2), extruded E460 (b1, b2), and coated CE460 (c1, c2) specimens.

are 310 ± 17 MPa, 321 ± 25 MPa, 11.1 ± 1.9 %, and 1.030 ± 0.017 mm y^{-1}, respectively. After the E460 specimen further fluoride coating treatment, the mechanical properties have little change. Nevertheless, the corrosion resistance increases remarkably, and its average corrosion rate decreases from 1.030 ± 0.017 to 0.070 ± 0.004 mm y^{-1}.

Acknowledgements

This work was supported by the Natural Science Foundation of Henan Province (242300420018), the Provincial and Ministerial Co-construction of Collaborative Innovation Center for Non-ferrous Metal New Materials and Advanced Processing Technology, and the Henan Key Laboratory of Non-ferrous Materials Science and Processing Technology.

References

[1] J. Nagels, M. Stokdijk, P. M. Rozing, Stress shielding and bone resorption in shoulder arthroplasty, Journal of Shoulder and Elbow Surgery 12 (2003) 35–39. https://doi.org/10.1067/mse.2003.22

[2] J. Zhou, Q. Li, H. Zhang, F. Chen, Corrosion behavior of AZ91D magnesium alloy in three different physiological environments, J. of Mater. Eng. and Perform. 23 (2014) 181–186. https://doi.org/10.1007/s11665-013-0751-4

[3] J. Li, L. Tan, P. Wan, X. Yu, K. Yang, Study on microstructure and properties of extruded Mg–2Nd–0.2Zn alloy as potential biodegradable implant material, Materials Science and Engineering C 49 (2015) 422–429. https://doi.org/10.1016/j.msec.2015.01.029

[4] W. Jiang, D. Wu, W. Dong, J. Ding, Z. Ye, P. Zeng, Y. Gao, Design and validation of a nonparasitic 2R1T parallel hand-held prostate biopsy robot with remote center of motion, Journal of Mechanisms and Robotics 16 (2024) 051009. https://doi.org/10.1115/1.4062793

[5] Y. Chen, J. Dou, H. Yu, C. Chen, Degradable magnesium-based alloys for biomedical applications: The role of critical alloying elements, J. Biomater. Appl. 33 (2019) 1348–1372. https://doi.org/10.1177/0885328219834656

[6] C. Cai, R. Song, L. Wang, J. Li, Surface corrosion behavior and reaction product film deposition mechanism of Mg-Zn-Zr-Nd alloys during degradation process in Hank's solution, Surface and Coatings Technology 342 (2018) 57–68. https://doi.org/10.1016/j.surfcoat.2018.02.085

[7] W. Zhou, T. Shen, N. N. Aung, Effect of heat treatment on corrosion behavior of magnesium alloy AZ91D in simulated body fluid, Corrosion Science 52 (2010) 1035–1041. https://doi.org/10.1016/j.corsci.2009.11.030

[8] Y. Liu, J. Wen, H. Yao, J. He, H. Li, Enhancing the corrosion resistance performance of Mg-1.8Zn-1.74Gd-0.5Y-0.4Zr biomaterial via solution treatment process, Materials 13 (2020) 836. https://doi.org/10.3390/ma13040836

[9] J. Chen, L. Tan, X. Yu, I. P. Etim, M. Ibrahim, K. Yang, Mechanical properties of magnesium alloys for medical application: A review, Journal of the Mechanical Behavior of Biomedical Materials 87 (2018) 68–79. https://doi.org/10.1016/j.jmbbm.2018.07.022

[10] Y. Ding, C. Wen, P. Hodgson, Y. Li, Effects of alloying elements on the corrosion behavior and biocompatibility of biodegradable magnesium alloys: A review, J. Mater. Chem. B 2 (2014) 1912–1933. https://doi.org/10.1039/C3TB21746A

[11] F. Xing, F. Guo, J. Su, X. Zhao, H. Cai, The existing forms of Zr in Mg-Zn-Zr magnesium alloys and its grain refinement mechanism, Mater. Res. Express. 8 (2021) 066516. https://doi.org/10.1088/2053-1591/ac083c

[12] H. Yu, Y. Hongge, C. Jihua, B. Su, Y. Zheng, Y. Shen, Z. Ma, Effects of minor Gd addition on microstructures and mechanical properties of the high strain-rate rolled Mg–Zn–Zr alloys, Journal of Alloys and Compounds 586 (2014) 757–765. https://doi.org/10.1016/j.jallcom.2013.10.005

[13] L. Yang, N. Hort, D. Laipple, D. Höche, Y. Huang, K. U. Kainer, R. Willumeit, F. Feyerabend, Element distribution in the corrosion layer and cytotoxicity of alloy Mg–10Dy during in vitro biodegradation, Acta Biomaterialia 9 (2013) 8475–8487. https://doi.org/10.1016/j.actbio.2012.10.001

[14] H. Li, J. Wen, J. He, H. Shi, Y. Liu, Effects of Dy addition on the mechanical and degradation properties of Mg–2Zn–0.5Zr alloy, Advanced Engineering Materials 22 (2020) 1901360. https://doi.org/10.1002/adem.201901360

[15] T. T. Sasaki, K. Oh-ishi, T. Ohkubo, K. Hono, Enhanced age hardening response by the addition of Zn in Mg–Sn alloys, Scripta Materialia 55 (2006) 251–254. https://doi.org/10.1016/j.scriptamat.2006.04.005

[16] S. J. Meng, H. Yu, S. D. Fan, Q.-Z. Li, S. H. Park, J. S. Suh, Y. M. Kim, X.-L. Nan, M.-Z. Bian, F.-X. Yin, W.-M. Zhao, B. S. You, K. S. Shin, Recent progress and development in extrusion of rare earth free Mg alloys: A review, Acta Metall. Sin. (Engl. Lett.) 32 (2019) 145–168. https://doi.org/10.1007/s40195-018-00871-2

[17] Y. Song, E. H. Han, D. Shan, C. D. Yim, B. S. You, The effect of Zn concentration on the corrosion behavior of Mg–xZn alloys, Corrosion Science 65 (2012) 322–330. https://doi.org/10.1016/j.corsci.2012.08.037

[18] T. Li, L. H. Chai, S. H. Shi, Z. L. Xiang, Y. S. Cui, G. D. Shi, Z. Y. Chen, Effect of near-isothermal forging temperature on the microstructure and mechanical properties of near α high temperature titanium alloy, MSF 898 (2017) 579–585. https://doi.org/10.4028/www.scientific.net/MSF.898.579

[19] P. Wang, P. Xiong, J. Liu, S. Gao, T. Xi, Y. Cheng, A silk-based coating containing GREDVY peptide and heparin on Mg–Zn–Y–Nd alloy: improved corrosion resistance, hemocompatibility and endothelialization, J. Mater. Chem. B 6 (2018) 966–978. https://doi.org/10.1039/C7TB02784B

[20] G. E. J. Poinern, R. K. Brundavanam, X. T. Le, D. Fawcett, The mechanical properties of a porous ceramic derived from a 30 nm sized particle based powder of hydroxyapatite for potential hard tissue

engineering applications, AJBE 2 (2013) 278–286. https://doi.org/10.5923/j.ajbe.20120206.07
[21] S. Shadanbaz, G. J. Dias, Calcium phosphate coatings on magnesium alloys for biomedical applications: A review, Acta Biomaterialia 8 (2012) 20–30. https://doi.org/10.1016/j.actbio.2011.10.016
[22] H. Hornberger, S. Virtanen, A. R. Boccaccini, Biomedical coatings on magnesium alloys – A review, Acta Biomaterialia 8 (2012) 2442–2455. https://doi.org/10.1016/j.actbio.2012.04.012
[23] R. Zeng, L. Cui, W. Ke, Biomedical magnesium alloys: Composition, microstructure and corrosion, Acta Metall. Sin. 54 (2018) 1215–1235. https://doi.org/10.11900/0412.1961.2018.00032
[24] L. Mao, L. Shen, J. Chen, Y. Wu, M. Kwak, Y. Lu, Q. Xue, J. Pei, L. Zhang, G. Yuan, R. Fan, J. Ge, W. Ding, Enhanced bioactivity of Mg–Nd–Zn–Zr alloy achieved with nanoscale MgF_2 surface for vascular stent application, ACS Appl. Mater. Interfaces 7 (2015) 5320–5330. https://doi.org/10.1021/am5086885
[25] Z. Li, S. Sun, M. Chen, B. D. Fahlman, D. Liu, H. Bi, In vitro and in vivo corrosion, mechanical properties and biocompatibility evaluation of MgF_2-coated Mg-Zn-Zr alloy as cancellous screws, Materials Science and Engineering C 75 (2017) 1268–1280. https://doi.org/10.1016/j.msec.2017.02.168
[26] U. Riaz, Z. Rahman, H. Asgar, U. Shah, I. Shabib, W. Haider, An insight into the effect of buffer layer on the electrochemical performance of MgF_2 coated magnesium alloy ZK60, Surface and Coatings Technology 344 (2018) 514–521. https://doi.org/10.1016/j.surfcoat.2018.03.081
[27] H. Li, J. Wen, Y. Liu, J. He, H. Shi, P. Tian, Progress in research on biodegradable magnesium alloys: A review, Advanced Engineering Materials 22 (2020) 2000213. https://doi.org/10.1002/adem.202000213
[28] S. Zhou, L. Liu, N. Huang, Effect of extrusion ratio on microstructure, mechanical and degradation properties of Mg-2Zn-0.2Mn biomedical alloy, Integrated Ferroelectrics 154 (2014) 166–174. https://doi.org/10.1080/10584587.2014.904713
[29] Z. Huang, W. Qi, K. Zheng, X. M. Zhang, M. Liu, Z. M. Yu, J. Xu, Microstructures and mechanical properties of Mg–Zn–Zr–Dy wrought magnesium alloys, Bull. Mater. Sci. 36 (2013) 437–445. https://doi.org/10.1007/s12034-013-0469-9
[30] P. Mohan Sathyaraj, K. Ravichandran, T. S. N. Sankara Narayanan, Controlling the rate of degradation of Mg using magnesium fluoride and magnesium fluoride-magnesium phosphate duplex coatings, Journal of Magnesium and Alloys 10 (2022) 295–312. https://doi.org/10.1016/j.jma.2021.06.005
[31] T. Yan, L. Tan, D. Xiong, X. Liu, B. Zhang, K. Yang, Fluoride treatment and in vitro corrosion behavior of an AZ31B magnesium alloy, Materials Science and Engineering C 30 (2010) 740–748. https://doi.org/10.1016/j.msec.2010.03.007
[32] S. Ghaedi Faramoushjani, F. Chinaei, H. R. Bakhsheshi-Rad, M. Hasbullah Idris, Effect of fluoride conversion coating on corrosion of behavior of Mg-Ca-Zn alloy, Advanced Materials Research 712–715 (2013) 3–6. https://doi.org/10.4028/www.scientific.net/AMR.712-715.3
[33] J. Chen, X. Zhu, L. Tan, K. Yang, X.-P. Su, Effects of ECAP extrusion on the microstructure, mechanical properties and biodegradability of Mg–2Zn–xGd–0.5Zr alloys, Acta Metall. Sin. (Engl. Lett.) 34 (2021) 205–216. https://doi.org/10.1007/s40195-020-01136-7
[34] H. Yao, X. Zha, Y. Xiong, S. Wang, M. Huttula, W. Cao, Stress corrosion cracking behavior of an as-extruded Mg-1.8 Zn-0.5 Zr-1.5 Gd magnesium alloy in a simulated body fluid, Kovove Mater. 60 (2022) 327–340. https://doi.org/10.31577/km.2022.5.327
[35] X. Cao, Z. Zhang, C. Xu, C. Ren, W. Yang, J. Zhang, Micro-galvanic corrosion behavior and mechanical properties of extruded Mg-2Y-1Zn-0.4Zr-0.3Sr alloys with different extrusion temperament immersed in simulated body fluids, Materials Chemistry and Physics 271 (2021) 124928. https://doi.org/10.1016/j.matchemphys.2021.124928
[36] Y. S. Jeong, W. J. Kim, Enhancement of mechanical properties and corrosion resistance of Mg–Ca alloys through microstructural refinement by indirect extrusion, Corrosion Science 82 (2014) 392–403. https://doi.org/10.1016/j.corsci.2014.01.041
[37] M. Esmaily, J. E. Svensson, S. Fajardo, N. Birbilis, G. S. Frankel, S. Virtanen, R. Arrabal, S. Thomas, L. G. Johansson, Fundamentals and advances in magnesium alloy corrosion, Progress in Materials Science 89 (2017) 92–193. https://doi.org/10.1016/j.pmatsci.2017.04.011
[38] M. Jiang, C. Xu, H. Yan, S. H. Lu, T. Nakata, C. S. Lao, R. S. Chen, S. Kamado, E. H. Han, Correlation between dynamic recrystallization and formation of rare earth texture in a Mg-Zn-Gd magnesium alloy during extrusion, Sci. Rep. 8 (2018) 16800. https://doi.org/10.1038/s41598-018-35170-4
[39] Z. Gui, Z. Kang, Y. Li, Mechanical and corrosion properties of Mg-Gd-Zn-Zr-Mn biodegradable alloy by hot extrusion, Journal of Alloys and Compounds 685 (2016) 222–230. https://doi.org/10.1016/j.jallcom.2016.05.241
[40] H. Li, J. Wen, Y. Liu, J. He, Enhancement of mechanical properties and corrosion resistance of Mg–2Zn–0.5Zr–1.5Dy (mass%) alloy by a combination of heat treatment and hot extrusion, Materials and Corrosion 73 (2022) 587–601. https://doi.org/10.1002/maco.202112755
[41] P. Chakraborty Banerjee, S. Al-Saadi, L. Choudhary, S. E. Harandi, R. Singh, Magnesium implants: Prospects and challenges, Materials 12 (2019) 136. https://doi.org/10.3390/ma12010136
[42] T. Long, X. Zhang, Q. Huang, L. Liu, Y. Liu, J. Ren, Y. Yin, D. Wu, H. Wu, Novel Mg-based alloys by selective laser melting for biomedical applications: microstructure evolution, microhardness and in vitro degradation behavior, Virtual and Physical Prototyping 13 (2018) 71–81. https://doi.org/10.1080/17452759.2017.1411662
[43] H. Y. Choi, W. J. Kim, Effect of thermal treatment on the bio-corrosion and mechanical properties of ultrafine-grained ZK60 magnesium alloy, Journal of the Mechanical Behavior of Biomedical Materials 51 (2015) 291–301. https://doi.org/10.1016/j.jmbbm.2015.07.019

[44] K. D. Ralston, N. Birbilis, Effect of grain size on corrosion: A review, Corrosion 66 (2010) 075005–13. https://doi.org/10.5006/1.3462912
[45] D. Liu, C. Guo, L. Chai, V. R. Sherman, X. Qin, Y. Ding, M. A. Meyers, Mechanical properties and corrosion resistance of hot extruded Mg–2.5Zn–1Ca alloy, Materials Science and Engineering B 195 (2015) 50–58. https://doi.org/10.1016/j.mseb.2015.02.001
[46] M. Alvarez-Lopez, M. D. Pereda, J. A. Del Valle, M. Fernandez-Lorenzo, M. C. Garcia-Alonso, O. A. Ruano, M. L. Escudero, Corrosion behaviour of AZ31 magnesium alloy with different grain sizes in simulated biological fluids, Acta Biomaterialia 6 (2010) 1763–1771. https://doi.org/10.1016/j.actbio.2009.04.041
[47] G. R. Argade, S. K. Panigrahi, R. S. Mishra, Effects of grain size on the corrosion resistance of wrought magnesium alloys containing neodymium, Corrosion Science 58 (2012) 145–151. https://doi.org/10.1016/j.corsci.2012.01.021
[48] N. N. Aung, W. Zhou, Effect of grain size and twins on corrosion behaviour of AZ31B magnesium alloy, Corrosion Science 52 (2010) 589–594. https://doi.org/10.1016/j.corsci.2009.10.018
[49] L. Li, C. Zhang, H. Lv, C. Liu, Z. Wen, J. Jiang, Texture development and tensile properties of Mg–Yb binary alloys during hot extrusion and subsequent annealing, Journal of Magnesium and Alloys 10 (2022) 249–265. https://doi.org/10.1016/j.jma.2021.05.001
[50] D. Song, A. Ma, J. Jiang, P. Lin, D. Yang, J. Fan, Corrosion behavior of equal-channel-angular-pressed pure magnesium in NaCl aqueous solution, Corrosion Science 52 (2010) 481–490. https://doi.org/10.1016/j.corsci.2009.10.004
[51] G. B. Hamu, D. Eliezer, L. Wagner, The relation between severe plastic deformation microstructure and corrosion behavior of AZ31 magnesium alloy, Journal of Alloys and Compounds 468 (2009) 222–229. https://doi.org/10.1016/j.jallcom.2008.01.084
[52] S. H. Kayani, S. Park, K. Euh, J. B. Seol, J. G. Kim, H. Sung, Dislocation-aided electrochemical behavior of precipitates in stress corrosion cracking of Al–Zn–Mg–Cu alloys, Materials Characterization 190 (2022) 112019. https://doi.org/10.1016/j.matchar.2022.112019
[53] Y. Xiong, Z. Yang, T. Zhu, Y. Jiang, Effect of texture evolution on corrosion resistance of AZ80 magnesium alloy subjected to applied force in simulated body fluid, Materials Research Express 7 (2020) 015406. https://doi.org/10.1088/2053-1591/ab648c
[54] T. Hosaka, S. Yoshihara, I. Amanina, B. J. MacDonald, Influence of grain refinement and residual stress on corrosion behavior of AZ31 magnesium alloy processed by ECAP in RPMI-1640 medium, Procedia Engineering 184 (2017) 432–441. https://doi.org/10.1016/j.proeng.2017.04.114
[55] L. Lin, Z. Liu, W. Zhuang, H. Peng, Effects of prestrain on the surface residual stress and corrosion behavior of an Al-Zn-Mg-Cu alloy plate, Materials Characterization 160 (2020) 110129. https://doi.org/10.1016/j.matchar.2020.110129
[56] D. Ahmadkhaniha, M. Fedel, H. Meydarzadeh Sohi, F. Deflorian, Corrosion behavior of severely plastic deformed magnesium based alloys: A review, Surf. Eng. Appl. Electrochem. 53 (2017) 439–448. https://doi.org/10.3103/S1068375517050039
[57] M. Ascencio, M. Pekguleryuz, S. Omanovic, An investigation of the corrosion mechanisms of WE43Mg alloy in a modified simulated body fluid solution: The effect of electrolyte renewal, Corrosion Science 91 (2015) 297–310. https://doi.org/10.1016/j.corsci.2014.11.034
[58] Z. Li, M. Chen, W. Li, H. Zheng, C. You, D. Liu, F. Jin, The synergistic effect of trace Sr and Zr on the microstructure and properties of a biodegradable Mg-Zn-Zr-Sr alloy, Journal of Alloys and Compounds 702 (2017) 290–302. https://doi.org/10.1016/j.jallcom.2017.01.178
[59] L. Chen, Y. Sheng, X. Wang, X. Zhao, H. Liu, W. Li, Effect of the microstructure and distribution of the second phase on the stress corrosion cracking of biomedical Mg-Zn-Zr-xSr alloys, Materials 11 (2018) 551. https://doi.org/10.3390/ma11040551
[60] Q. Li, X. Liu, T. Yan, L. Tan, B. Zhang, K. Yang, Effect of fluoride conversion treatment on bio-corrosion behavior of AZ31B magnesium alloy, Rare Metal Mat. Eng. 40 (2011) 1859–1863. https://doi.org/10.12442/j.issn.1002-185X.011.40.10.18591863
[61] J. Wang, J. Li, Y. Zhang, W. Yu, Effects of the addition of micro-amounts of calcium on the corrosion resistance of Mg-0.1Mn-1.0Zn-xCa biomaterials, J. of Mater. Eng. and Perform. 28 (2019) 1553–1562. https://doi.org/10.1007/s11665-019-03958-8
[62] J. Wen, J. He, X. Lu, Influence of silicon on the corrosion behaviour of Al–Zn–In–Mg–Ti sacrificial anode, Corrosion Science 53 (2011) 3861–3865. https://doi.org/10.1016/j.corsci.2011.07.039
[63] T. C. Yeh, T. Huang, H. Huang, Y.-P. Huang, Y.-T. Cai, S.-T. Lin, Y. Wei, J.-M. Yeh, Electrochemical investigations on anticorrosive and electrochromic properties of electroactive polyurea, Polym. Chem. 3 (2012) 2209–2216. https://doi.org/10.1039/C2PY20061A
[64] Z. Shi, A. Atrens, An innovative specimen configuration for the study of Mg corrosion, Corrosion Science 1 (2011) 226–246. https://doi.org/10.1016/j.corsci.2010.09.016
[65] A. D. King, N. Birbilis, J. R. Scully, Accurate electrochemical measurement of magnesium corrosion rates: A combined impedance, mass-loss and hydrogen collection study, Electrochimica Acta 121 (2014) 394–406. https://doi.org/10.1016/j.electacta.2013.12.124
[66] J. He, J. Wen, X. Li, Effects of precipitates on the electrochemical performance of Al sacrificial anode, Corrosion Science 53 (2011) 1948–1953. https://doi.org/10.1016/j.corsci.2011.02.016
[67] Y. Xiong, T. Zhu, J. Yang, Y. Yu, X. Gong, Effect of twin-induced texture evolution on corrosion resistance of extruded ZK60 magnesium alloy in simulated body fluid, J. of Mater. Eng. and Perform. 29 (2020) 5710–5717. https://doi.org/10.1007/s11665-020-05068-2
[68] J. He, J. Wen, X. Li, G.-W. Wang, C.-H. Xu, Influence of Ga and Bi on electrochemical performance of Al-Zn-Sn sacrificial anodes, Transactions of Nonferrous Metals Society of China 21 (2011) 1580–1586. https://doi.org/10.1016/S1003-6326(11)60900-X
[69] Y. Zhang, J. Li, J. Li, Microstructure, mechanical properties, corrosion behavior and film formation mechanism of Mg-Zn-Mn-xNd in Kokubo's solution, Journal of Alloys Compounds 730 (2017) 458–470. https://doi.org/10.1016/j.jallcom.2017.09.325

[70] Z. Gui, Z. Kang, Y. Li, Corrosion mechanism of the as-cast and as-extruded biodegradable Mg-3.0Gd-2.7Zn-0.4Zr-0.1Mn alloys, Materials Science and Engineering C 96 (2019) 831–840. https://doi.org/10.1016/j.msec.2018.11.037